

For later use we note that the vertical log-pressure velocity $w = Dz/Dt$ is related to the vertical p -velocity $\omega = Dp/Dt$ by $\omega = -p_0 e^{-z} w$.

2.5 Solutions

All the model results shown in this section have been constructed by numerical evaluation of (2.41), and (2.42), which involves a superposition of zonal wavenumbers (sum over m), meridional wavenumbers (sum over n), and wave types (sum over r). In our examples the spectral coefficients $\hat{\eta}_{mnr}$ decay exponentially with n for all choices of m , which enables us to truncate the spectral solution at $n = N$ with a specified degree of accuracy. In general, $N = 200$ gives accurate results. Appendix F displays a flow chart outlining the procedure for computing the solutions.

Although the solutions have been computed over the entire zonal domain, only half the domain, centered on the forcing, is shown. This allows greater detail to be displayed for the region nearest the forcing. Using the parameters listed in Table 2.1, the 850 hPa wind and geopotential fields computed from (2.41) are shown in the top panel of Fig. 2.5 for $y_0 = 0$ and in the top panel of Fig. 2.7 for $y_0 = 450$ km. The choice of 850 hPa as the display level is arbitrary. According to the profile of $Z(z)$ shown in Fig. 2.1, upper tropospheric fields have the opposite sign and approximately twice the magnitude of the lower tropospheric fields. An interesting property of these simple linear solutions is that the lower tropospheric maximum westerly winds in the wake of the convective envelope are stronger than the lower tropospheric maximum easterly winds ahead of the convection. For example, in Fig. 2.5 the maximum 850 hPa westerly flow is 3.7 m s^{-1} while the maximum easterly flow is 1.6 m s^{-1} . In Fig. 2.7 the corresponding values are 4.2 m s^{-1} and 1.4 m s^{-1} . These wind speeds, the degree of asymmetry between westerlies and easterlies, and the larger zonal extent of the easterlies compared to the westerlies all agree well with the observed MJO composite ³

³ There is substantial variability in the cases that make up the MJO composite so that a detailed comparison of model results with an individual MJO case probably requires modeling the details of the diabatic forcing associated with that case.

(see Figs. 1.4 and 1.5) presented by Kiladis et al. (2005, Figs. 2 and 3). The remaining panels of Figs. 2.5 show the decomposition of the total fields into Rossby modes ($r = 0$ with $n \geq 1$), inertia-gravity modes ($r = 1, 2$ with $n \geq 1$ and $r = 2$ with $n = 0$), and Kelvin modes ($r = 2$ with $n = -1$). We have not plotted the contribution from mixed Rossby-gravity modes ($r = 0$ with $n = 0$) since it vanishes when $y_0 = 0$. The remaining panels in Fig. 2.7 show the same components as in Fig. 2.5, but also present is the mixed Rossby-gravity mode because it is nonzero when $y_0 \neq 0$. It should be noted that for small displacements off the equator the mixed Rossby-gravity response is negligible compared with the other components and was shown here only for completeness. The 395 hPa vertical motion field (recall that $Z'(z)$ reaches its maximum amplitude at $p \approx 395$ hPa) computed from (2.42) is shown in the top panel of Fig. 2.6 for $y_0 = 0$ and in the top panel of Fig. 2.8 for $y_0 = 450$ km. The other panels of Figs. 2.6 and 2.8 show the same components for the vertical motion field as were shown of the circulation in Figs. 2.5 and 2.7, respectively. These figures show that the vertical motion field is primarily composed of the Kelvin and inertia-gravity response as the Rossby vertical motion is very small for any value of y_0 , and the mixed-Rossby gravity response is identically zero on the equator, and relatively small otherwise.

Some notable features are apparent from Figs. 2.5–2.8. The total u, v, ϕ fields are composed of Rossby waves on the west side of the source, Kelvin waves on the east side, with “slaved” inertia-gravity waves providing low-level convergence near the source. As the center of the convective envelope is shifted north of the equator there is very little change in the response east of the forcing. In contrast, the response west of the forcing becomes biased to the northern hemisphere.

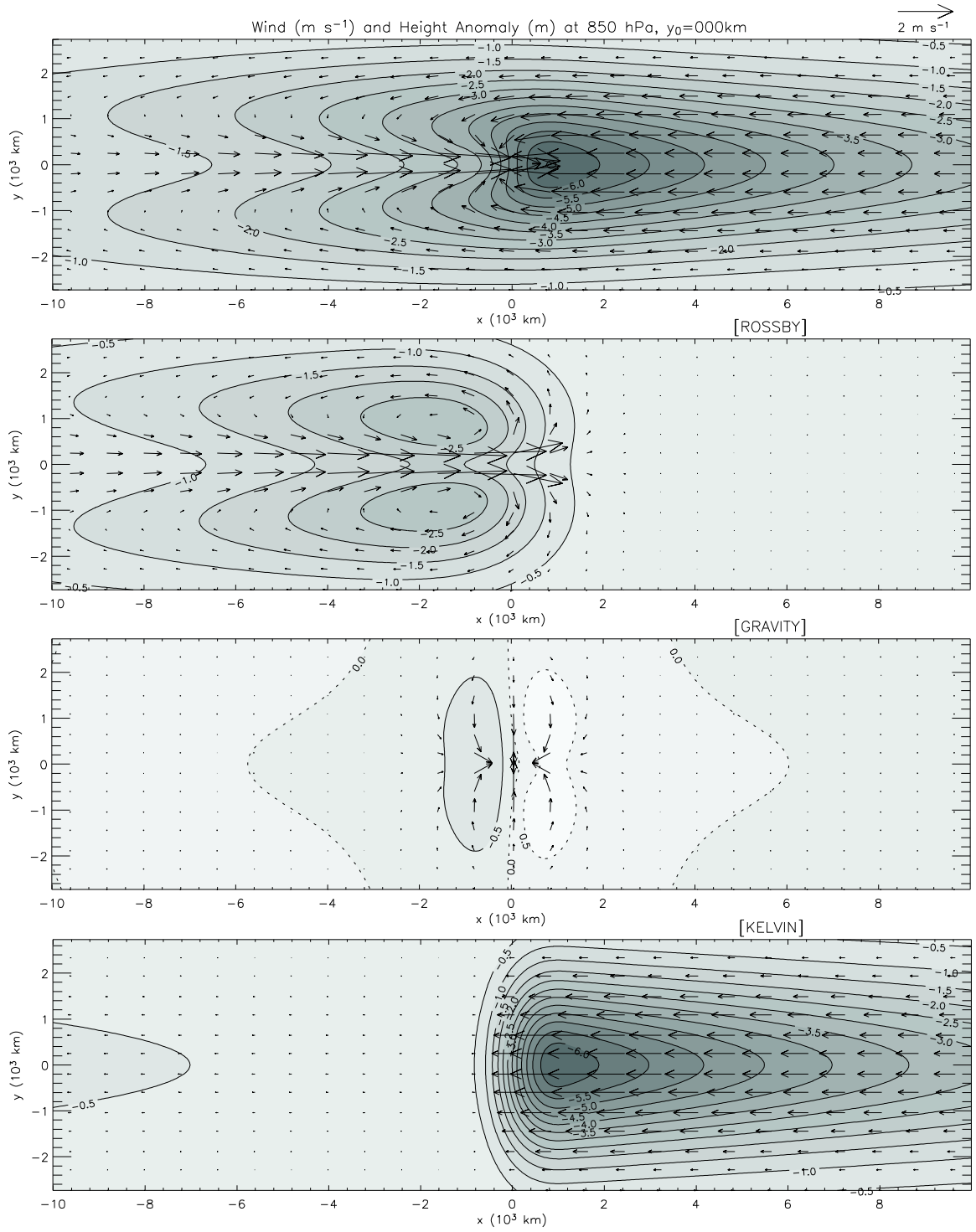


Figure 2.5: The upper panel shows the geopotential height anomaly and winds at 850 hPa for $y_0 = 0$ and for the remaining parameters listed in Table 2.1. The remaining three panels show respectively the contributions made by Rossby waves, inertia-gravity waves, and Kelvin waves.

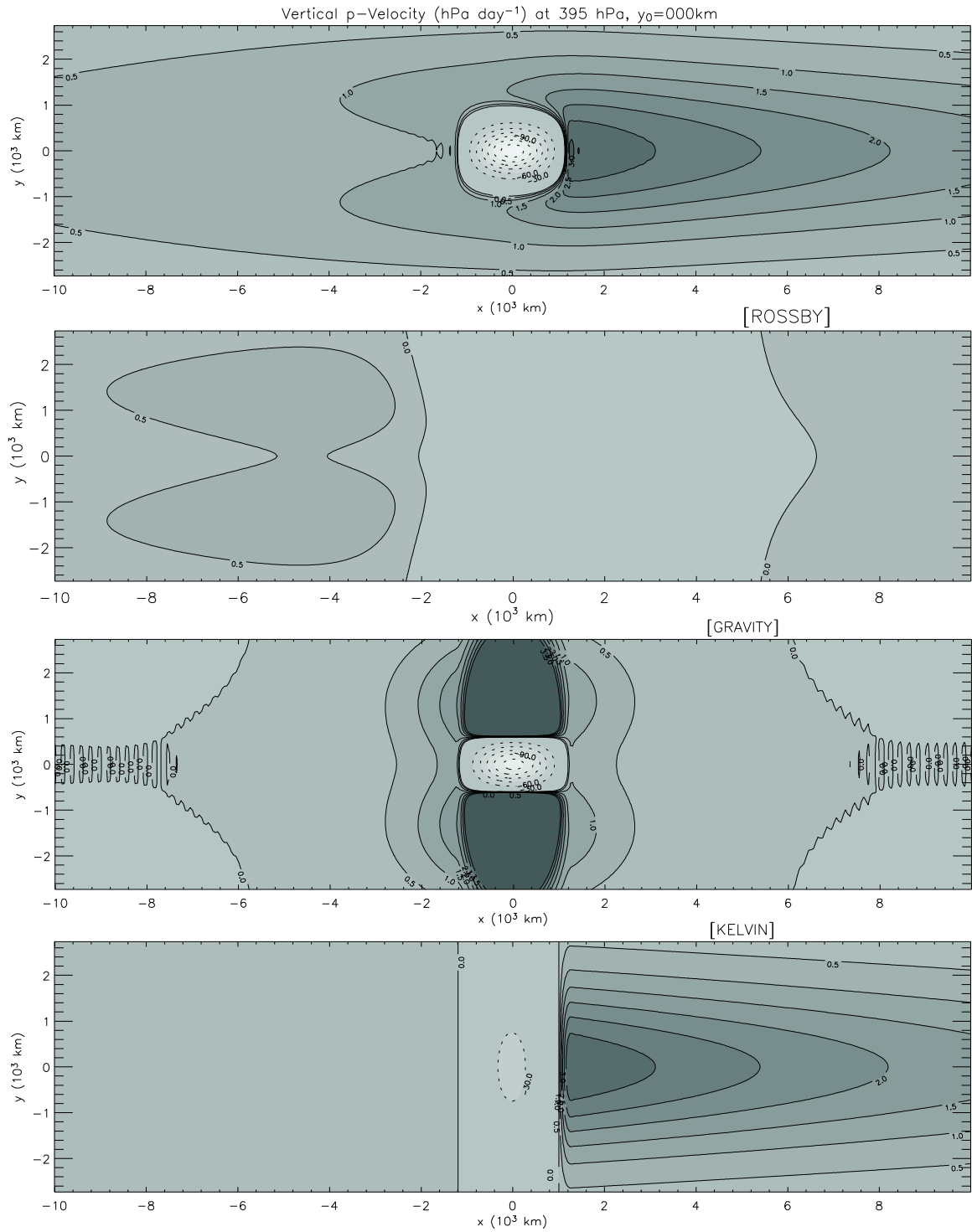


Figure 2.6: The first panel shows the vertical p -velocity, ω , at 395 hPa, with a contour interval of 30 hPa day⁻¹ in the region of rising motion (dashed contours), and a contour interval of 0.5 hPa day⁻¹ in the region of sinking motion (solid contours). The remaining panels show respective contributions of Rossby waves, inertia-gravity waves, and Kelvin waves to the vertical motion field. Results in this figure are for $y_0 = 0$.

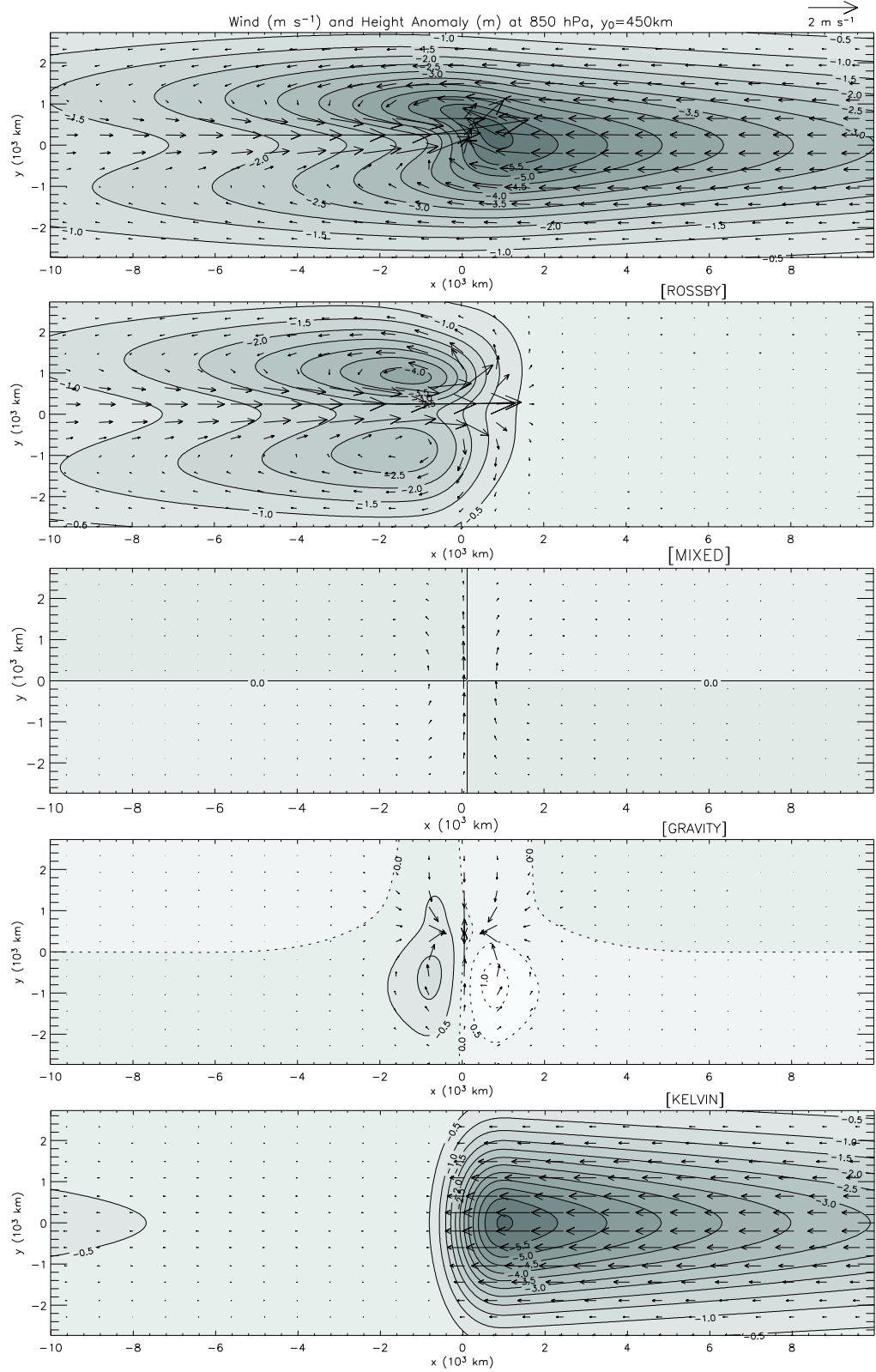


Figure 2.7: Same as Fig. 2.5, but the center of the convective forcing is shifted north of the equator ($y_0 = 450\text{ km}$), so the nonzero mixed Rossby-gravity component is shown as well.

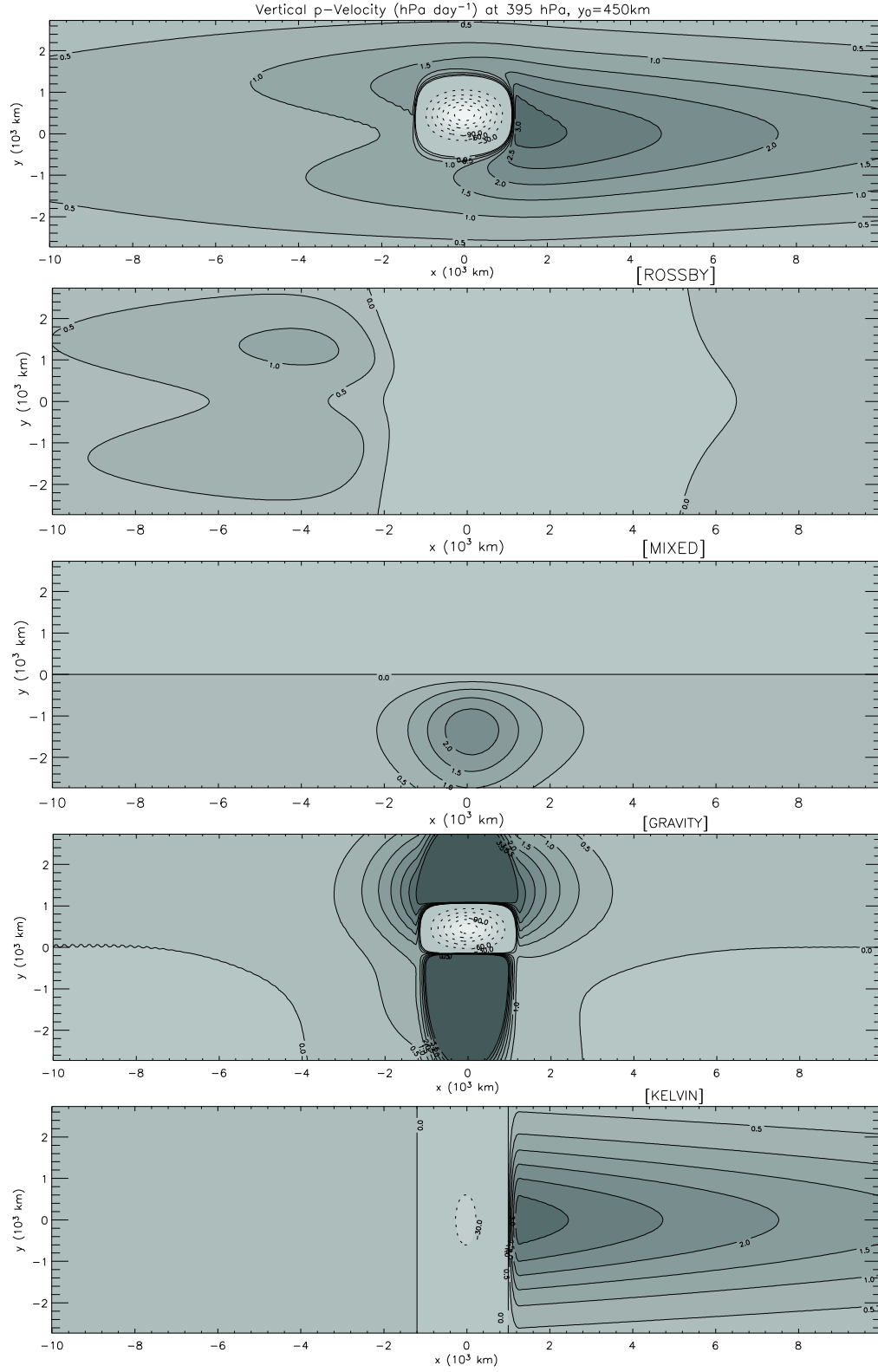


Figure 2.8: Same as Fig. 2.6, but the center of the convective forcing is shifted north of the equator ($y_0 = 450$ km), so the nonzero mixed Rossby-gravity component is shown as well.